HEALTH AND MEDICINE

Hybridized and engineered microbe for catalytic generation of peroxynitrite and cancer immunotherapy under sonopiezo initiation

Liping Wang[1,2]†, Penghao Ji[3]†, Jiadie Yu[3], Shuwen Qiu[3], Bolin An[4,5], Minfeng Huo[3]*, Jianlin Shi[1,2]*

Living therapeutics is an emerging antitumor modality by living microorganisms capable of selective tropism and effective therapeutics. Nevertheless, primitive microbes could only present limited therapeutic functionalities against tumors. Hybridization of the microbes with multifunctional nanocatalysts is of great significance to achieve enhanced tumor catalytic therapy. In the present work, nitric oxide synthase (NOS)–engineered *Escherichia coli* strain MG1655 (NOBac) was used to hybridize with the sonopiezocatalytic $BaTiO_3$ nanoparticles (BTO NPs) for efficient tumor-targeted accumulation and antitumor therapy. Under ultrasound irradiation, superoxide anions created by the piezocatalytic reaction of BTO NPs could immediately react with nitric oxide (NO) generated from NOBac to produce highly oxidative peroxynitrite $ONOO^-$ species in cascade, resulting in robust tumor piezocatalytic therapeutic efficacy, prompting prominent and sustained antitumoral immunoactivation simultaneously. The present work presents a promising cancer immunotherapy based on the engineered and hybridized microbes for highly selective and sonopiezo-controllable tumor catalytic therapy.

INTRODUCTION

Living therapy is an emerging therapy to treat sustained or chronic diseases in the frontier of biomedical engineering, by exploiting the advantages of the design controllability, multifunctionality, and sophisticated sensitivity of the living cells for multiple medical purposes (*1*–*3*). Living therapeutics makes use of native or biologically engineered microorganisms, yeasts, and eukaryotes, which are capable of producing therapeutic substances or agents, modulating the pathological microenvironment to heal the disease (*4*–*6*). For instance, malignant tumors harbor complicated genetic and molecular microenvironments including characteristic hypoxic features, aggressive blood supply, intense immunosuppression, and the ability to capture nutrients from adjacent tissues (*7*). Upon administration, these living microbes could selectively colonize and proliferate inside the tumor region, presenting pronounced organ selectivity with a tumor/liver accumulation ratio of higher than 1000:1, conferring the tumor-targeting performance of the living microbes with obligate or facultative anaerobes (*8*, *9*). With the advances of synthetic biology, these living microbes can be further genetically modified to secrete therapeutic agents to intervene the progression of tumor. For instance, after genetic engineering, histone-like protein A expressed on the surface of *Escherichia coli* enables these microbes to target the colorectal cancer cells. When a cruciferous vegetable diet was given, the myrosinase secreted by the microbes will effectively convert the glucosinolate into sulforaphane to generate an anticancer effect, resulting in satisfactory tumor suppression consequence (*10*). In another report, Chen and coworkers (*11*) constructed the engineered *Staphylococcus epidermidis* that can express tumor antigens after colonization in tumor tissues, specifically initiating T cell responses against melanoma. Bacterial strain *Salmonella typhimurium* could also be modified to secrete *Vibrio vulnificus* flagellin B, inducing potent immune responses in diverse types of tumor (*12*). These studies have made living microbes the most promising candidates for biomedical therapeutics.

Hybridization of the living microbes with synthetic components can further deliver versatile therapeutic functionalities to the targeted region, enabling multiple interactions for unprecedented therapeutic opportunities as compared to the unhybridized living microbes (*13*, *14*). For example, Alapan and coworkers (*15*) conjugated red blood cell (RBC)–containing superparamagnetic iron oxide nanoparticles to *E. coli* MG1655 to obtain biohybrid microswimmers. With the autonomous and propulsive performance of bacteria, these microswimmers can deliver cargo to the designated location under the guidance of the magnetic field. Excessive bacteria could be eliminated by a light-activated hyperthermia. In addition, Zheng and coworkers (*16*) engineered the nitric oxide (NO)–generating enzymes within *E. coli* and combined them with photocatalytic carbon nitride for light-initiated tumor therapy, leading to 80% suppression of tumor growth. Nevertheless, hybridized living microbes with light control suffer from the demerits of insufficient tissue penetration, deteriorating their therapeutic outcomes (*17*–*20*). Ultrasound (US) is a routine diagnostic and therapeutic irradiation source for diverse applications including imaging, thrombolysis, hyperthermia, and sonodynamic therapy (*21*–*24*). In the presence of nonsensitive molecules or nanomaterials, superoxide anion radicals could be generated. However, these radicals could be rapidly eliminated by superoxide dismutase, undermining the therapeutic outcome of the sonodynamic therapy. Peroxynitrite ($ONOO^-$) is a relatively

[1]State Key Laboratory of High Performance Ceramics and Superfine Microstructure, Shanghai Institute of Ceramics, Chinese Academy of Sciences; Research Unit of Nanocatalytic Medicine in Specific Therapy for Serious Disease, Chinese Academy of Medicine Science, Shanghai, 200050, P. R. China. [2]Center of Materials Science and Optoelectronics Engineering, University of Chinese Academy of Sciences, Beijing, 100049, P. R. China. [3]Shanghai Tenth People's Hospital, Shanghai Frontiers Science Center of Nanocatalytic Medicine, School of Medicine, Tongji University, Shanghai, 200072, P. R. China. [4]Center for Materials Synthetic Biology, Shenzhen Institute of Synthetic Biology, Shenzhen Institute of Advanced Technology, Chinese Academy of Sciences, Shenzhen, 518055, P. R. China. [5]CAS Key Laboratory of Quantitative Engineering Biology, Materials Synthetic Biology Center, Shenzhen Institute of Synthetic Biology, Shenzhen Institute of Advanced Technology, Chinese Academy of Sciences, Shenzhen, 518055, P. R. China.
*Corresponding author. Email: mfhuo@tongji.edu.cn (M.H.); jlshi@mail.sic.ac.cn (J.S.)
†These authors contributed equally to this work.

long-lived reactive nitrogen species (RNS) that could induce potent cell-killing efficacy against tumor, which is naturally generated by the radical reaction between superoxide anion radicals (O_2^-) and nitrogen monoxide (NO) (25). Through direct oxidation or free radical-mediated oxidation reactions (26, 27), $ONOO^-$ exhibits higher oxidative potentials than reactive oxygen species (ROS) such as hydroxyl radicals (28). Although the reaction between NO and O_2^- has a large reaction constant (~10^{10} M^{-1} s^{-1}) (29), these species could be easily eliminated by oxymyoglobin and superoxide dismutase under physiological conditions (30). Sustained intratumoral generation of $ONOO^-$ is therefore highly attractive for effective tumor therapeutics.

In this work, we initially genetically engineered tumor-targeting *E. coli* MG1655 microbes with bacterial nitric oxide synthase (bNOS) to form NO-producing living microbes NOBac (Fig. 1A). The NOBac was then hybridized with sonopiezosensitive $BaTiO_3$ nanoparticles (BTO NPs) to enable the oxidative peroxynitrite $ONOO^-$ production by the reaction between the superoxide anion radicals generated from BTO NPs under sonopiezo catalysis and NO gas molecules from NOBac. Meanwhile, upon tumor destruction, BTO NPs@NOBac can activate both the innate and adaptive immune responses inside tumor region, presenting the outperformed tumor curative strategy by hybridized engineering microbe.

RESULTS

Genetic engineering of NO generating microbe—NOBac

The NOS enzyme is able to catalyze the NO production from i-arginine. The gene encoding the bNOS isoform (CP019663.1) was amplified from *Bacillus subtilis* via polymerase chain reaction (PCR), which was further cloned into the pYTK001 plasmid with chloromycetin resistance (Fig. 1A and fig. S1). The integrated plasmid was then transformed into nonpathogenic facultative anaerobic *E. coli* MG1655 by heat shock, obtaining an engineered microbe featuring constitutive expression of bNOS enzyme and NO production capability—NOBac. Through colony PCR for NOBac, the band for bNOS gene could be detected to have a length of approximately 1000 bp, close to the theoretical size of 1092 bp (Fig. 1B). Compared to the non-engineered *E. coli* MG1655 strain (WTBac), a clear blot of bNOS protein (43 kDa) could be visualized for NOBac (Fig. 1C). The bioengineering of bNOS into the strain did not induce morphological change in the microbe (Fig. 1D), yet the latter phase of NOBac
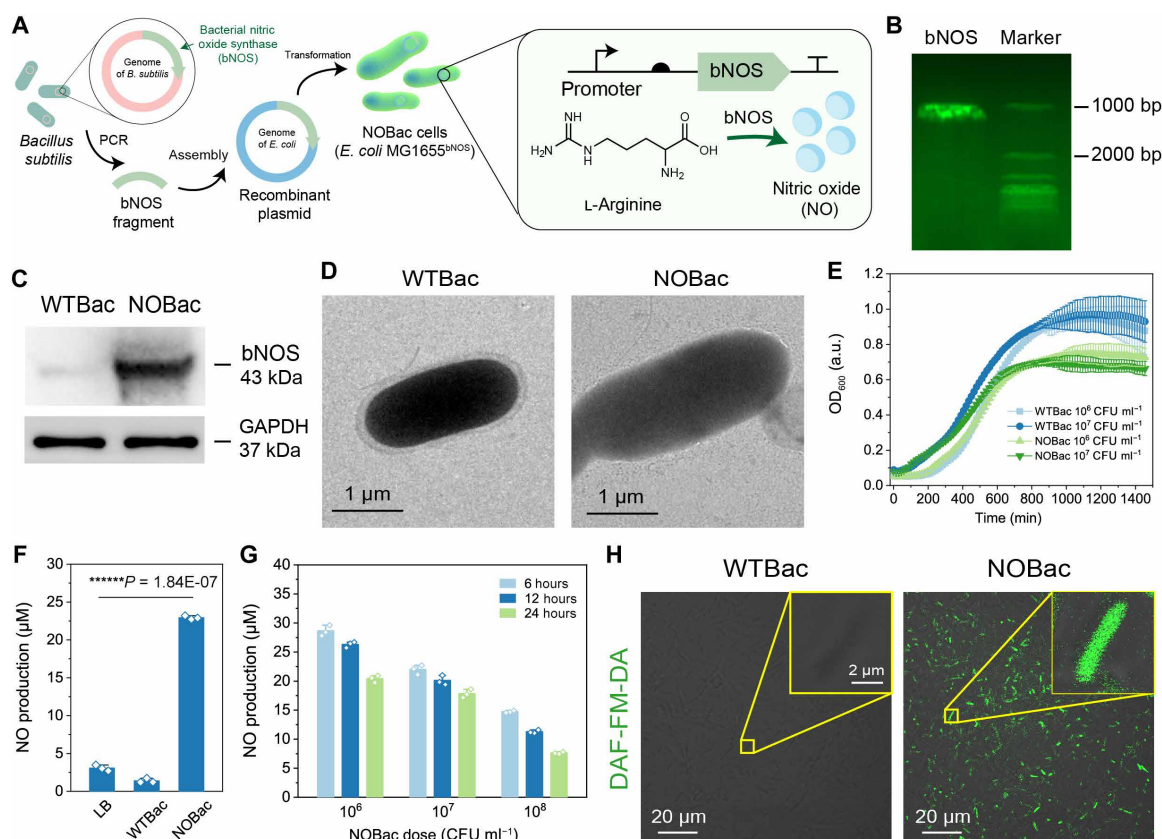
Fig. 1. Construction and characterization of NOBac. (**A**) Schematic diagram of the heterologous expression of bNOS from *E. coli* MG1655[bNOS] to generate NO molecules. (**B**) Photograph of Western blot result of *bNOS* gene. (**C**) Protein expression levels of bNOS and glyceraldehyde phosphate dehydrogenase (GAPDH) reference in WTBac and NOBac. (**D**) TEM images of WTBac and NOBac. (**E**) Growth curves of WTBac in LB broth and NOBac in LB broth containing chloromycetin (25 μg ml^{-1}) for 24 hours. Data are presented as mean ± SD. (**F**) NO production of LB broth containing different microbes (WTBac at the dose of 10^7 CFU ml^{-1} and NOBac at the dose of 10^7 CFU ml^{-1}) after 6 hours of incubation. Data are presented as they are and SD. $n = 3$. Significance is analyzed using the Student's t test. ******$P < 0.000001$. (**G**) NO productions of varied doses of NOBac in LB broth after varied time. Data are presented as they are and SD. $n = 3$. (**H**) Confocal images of NO probe DAF-FM-DA stained WTBac and NOBac. OD_{600}, optical density at 600 nm; a.u., arbitrary units.

growth was slightly inhibited (Fig. 1E), possibly due to the enhanced accumulation of the nitrite from generated NO. These evidences demonstrate the successful bioengineering of bNOS both genetically and transcriptionally.

We next evaluated the catalytic activity of bNOS by measuring the production of NO using Griess reagent, which measures the nitrites to reveal the generation of NO indirectly. First, at a dose concentration of 10^7 colony-forming units (CFU)/ml, we compared the NO generation between NOBac and WTBac, in reference to blank LB solution. Typically, a blank LB solution gives a basal NO production of 3.07 μM, while a supplementation of WTBac generates a lowered amount of NO (1.38 μM) since WTBac also consumes the nitrites. An identical dose of NOBac generates the greatly elevated NO amount of 22.9 μM, 15.6-fold higher than that generated by WTBac (Fig. 1F). Then, we investigate the NO generation by NOBac at three typical doses (10^6, 10^7, and 10^8 CFU/ml) at three time points (6, 12, and 24 hours). NOBac of 10^6 CFU/ml generates the highest NO amount of 28.6 μM in 6 hours, which then respectively decreases to 22.0 and 14.7 μM in 12 and 24 hours of incubation. Decreased NO amounts could also be observed for NOBac at increased doses to 10^7 and 10^8 CFU/ml (Fig. 1G). Since the microbe also consumes the nitrites for metabolism, it is reasonable for the observed time and dose dependences of the NO amounts. In addition, NOBac could be visualized by NO-specific fluorescence probe 3-amino, 4-aminomethyl-2′,7′-difluorofluorescein diacetate (DAF-FM DA). The green fluorescence was colocalized with the NOBac cells rather than with WTBac cells (Fig. 1H). The above results indicate that the bioengineering of bNOS endows NOBac with robust NO generation capacity.

Synthesis and characterizations of sonopiezosensitive BTO NPs

Perovskite-structured BTO NPs were synthesized by hydrothermal method (31, 32), followed by annealing at 800°C for 10 hours (Fig. 2A). From the x-ray diffraction pattern of the synthetic BTO NPs before and after annealing, we found that the non-annealed BTO NPs match well with cubic $BaTiO_3$ structure [Powder Diffraction File (PDF) #79-2263] with a space group of $Pm\bar{3}m$, which is a nonpiezoelectric space group (fig. S2). After annealing, BTO NPs become tetragonal-structured (PDF #05-0626) with piezoelectrically active $P4mm$ space group, showing characteristic peak splitting at 2θ = 45°, 75°, and 79° (Fig. 2B). The obtained tetragonal BTO NPs feature monodispersity and 98.9 nm, respectively, in transmission electron microscopy (TEM) imaging and hydrodynamic diameter on average (Fig. 2C and fig. S3), cuboid morphology (fig. S4), and uniform elemental distributions of Ba, O, and Ti (Fig. 2D). The high-resolution TEM image indicates the interplanar spacing (d_{hkl}) values of 0.412 and 0.402 nm, respectively, corresponding to the crystal plane (100) and (010) (Fig. 2E).
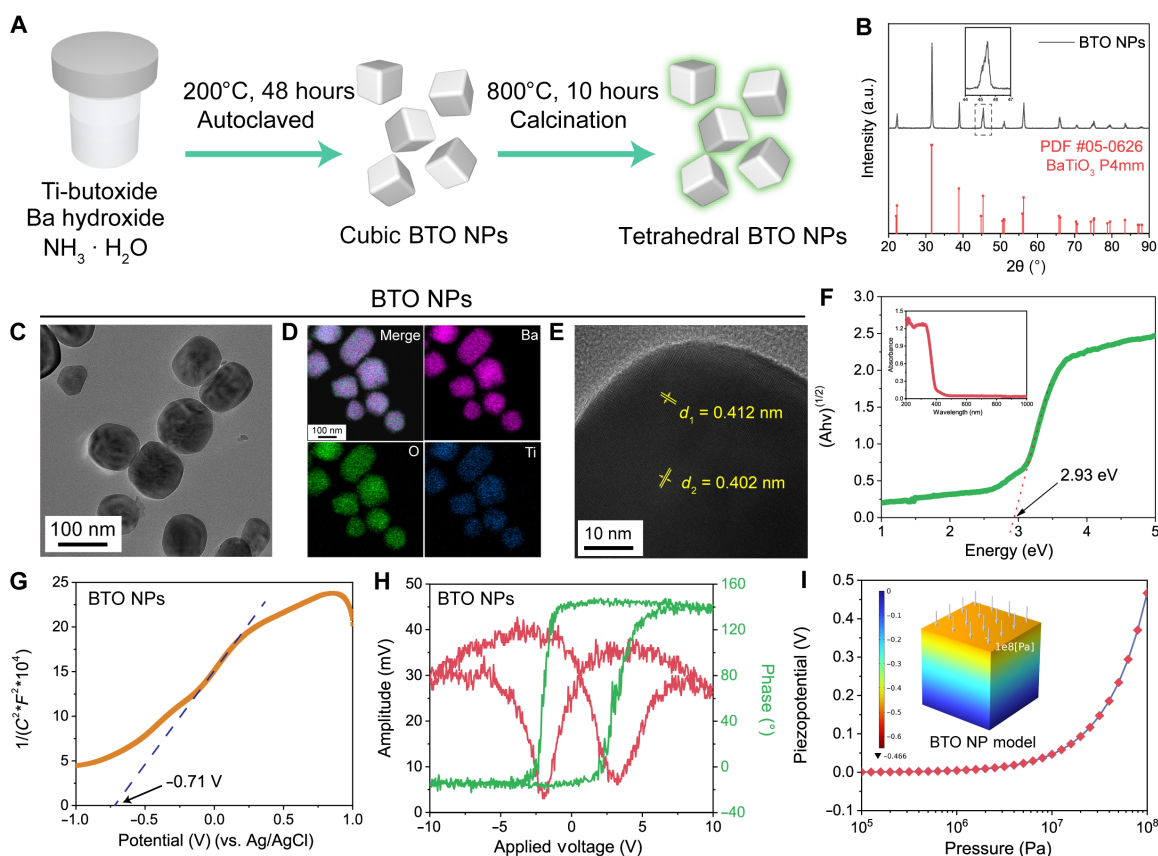
Fig. 2. Characterization of BTO nanoparticles. (**A**) Synthesis procedure of BTO nanoparticles. (**B**) XRD pattern of BTO nanoparticles. (**C**) TEM image of BTO nanoparticles. (**D**) Distribution of Ba, O, and Ti elements in BTO nanoparticles. (**E**) High-resolution TEM image of BTO NPs. (**F**) Bandgap diagram of BTO nanoparticles. The insert is UV-vis spectrum of BTO powders. (**G**) Mott-Schottky curve of BTO nanoparticles. (**H**) Amplitude curve and phase curve of BTO nanoparticles. (**I**) COMSOL model of the piezoelectric distribution of BTO nanoparticles under varied external pressures.

From Raman spectroscopy, the intensities of the characteristic peaks of B1 and E (TO + LO) at 304 cm^{-1} and A1 (TO) and E (TO) at 520 nm^{-1} of tetragonal-BTO are much higher than those of cubic BTO (fig. S5) (33), further confirming the tetragonal syngony of post-annealed BTO NPs. From x-ray photoelectron spectroscopy (XPS) result of BTO NPs, two characteristic peaks in high-resolution spectra of Ti positioned at 463.7 and 458.0 eV belong to Ti 2p$_{1/2}$ and Ti 2p$_{3/2}$, respectively. While the characteristic peaks in Ba positioned at 793.9 and 778.6 eV belong to Ba 3d$_{3/2}$ and Ba 3d$_{5/2}$. The XPS result indicates the dominant species of Ti^{4+} and Ba^{2+}, with an atomic ratio of 13.4:12.4 (fig. S6).

Sonopiezosensitive investigation of BTO NPs

Bulk BaTiO$_3$ has been demonstrated as a typical n-type wide band-gap semiconductor (34). For nanosized tetragonal BTO NPs, optical absorption could be observed from the ultraviolet-visible (UV-Vis) diffuse reflection spectrum. The absorption onset of BTO NPs was determined to be ~460 nm, corresponding to a wide bandgap of 2.93 eV (Fig. 2F). From Mott-Schottky tests, the electronic potential of BTO NPs was assayed to be −0.71 V (against the Ag/AgCl reference electrode). The calculated conduction band edge of BTO NPs is −0.51 V [against the normal hydrogen electrode (NHE)] according to the following Nernst equation (Eq. 1) (Fig. 2G). The valence band edge of BTO NPs was then obtained to be 2.42 V

$$E_{NHE} \text{ (V)} = E_{Ag/AgCl} + E^{o}_{Ag/AgCl} \qquad (1)$$

where E_{NHE} is the electronic potential in reference to NHE, $E_{Ag/AgCl}$ is the electronic potential in reference to the Ag/AgCl electrode, and $E^{o}_{Ag/AgCl}$ is the standard potential of the Ag/AgCl electrode at 298 K (0.198 V) (35).

We next used piezoresponse force microscopy to measure the piezoelectricity of BTO NPs. Classical butterfly amplitude curves and a phase loop close to a parallelogram could be observed, confirming the ferroelectricity performance of BTO NPs (Fig. 2H) (36). On the basis of the piezoelectric semiconducting feature, BTO NPs can achieve force-induced establishment of the built-in electric field (37). To investigate the potentials of the built-in electric field under specific mechanic pressure, finite element modeling simulation by COMSOL Multiphysics was used to evaluate the piezoelectricity of BTO NPs (38). We initially constructed cubic models of BTO NPs with their diameters ranging from 60 to 140 nm at an interval of 10 nm. When a pressure of 10^8 Pa was applied to the top surface of the NPs, increasing piezo potentials could be observed along with the increased nanoparticulate diameter (fig. S7, A to D). Typically, when cubic BTO NPs model with a diameter of 100 nm was selected, the applied pressure induced the piezopotentials in exponential behavior. Ambient pressure (10^5 Pa) leads to the liberal status of BTO NPs without induced built-in electric field and piezopotential. While under the applied pressure of 10^8 Pa, mimicking the presence of US irradiation (38), built-in electric field was generated, and the stimulated piezo potential of BTO NPs was calculated to be 0.466 V (Fig. 2I).

Since therapeutic US can induce localized sonomechanics up to 10^8 Pa, combining the sonomechanics and piezoelectricity could facilitate sonopiezo-controllable dynamic therapeutics in the biomedical frontier. According to the band structure of BTO NPs (E_{CB} = −0.51 V; E_{VB} = +2.42 V), the exited electrons have sufficient reduction potentials to reduce O$_2$ to generate superoxide anion radicals ($EO_2/\cdot O_2^-$ = −0.35 V). Nevertheless, the oxidation reaction from

H$_2$O to form hydroxyl radicals is forbidden (EH$_2$O/·OH = +2.73 V) (39). In the presence of sonomechanics generated from the therapeutic US, both conduction band (CB) and valence band (VB) will incline by a piezo potential of 0.466 V (Fig. 2I), leading to an instant CB$_i$ and VB$_i$ of −0.044 and +2.89 V, respectively, thermodynamically enabling the hydroxyl radical-generating oxidation reaction (Fig. 3A). To validate the theoretical calculations, bleaching of methylene blue (MB) was applied to investigate the sonopiezosensitive nature of BTO NPs (40). US irradiation of solution without BTO NPs leads to a minor bleach of MB (6.33%; fig. S8A). While for a typical assay solution containing MB (10 μg/ml) and BTO NPs (1 mg/ml), increased US irradiation power density from 0 to 2.0 W/cm^2 (t = 1 min) leads to gradually intensified bleaching of MB to 83.69% (fig. S8B) and a temperature rise by approximately 9 K (fig. S8C). To balance the minimized sonothermal effect and optimized sonopiezosensitivity, we used the US irradiation power density of 1.0 W/cm^2 for further investigation. It could be observed that US irradiation for serial time points induces the prominent degradation of the MB dye. A total of 64.6% of MB were bleached by the sonopiezosensitive performance of BTO NPs in 10 min under the US, validating the generation of the ROS by the sonopiezodynamic process of BTO NPs (Fig. 3B). These ROS were identified as hydroxyl radicals (·OH) and superoxide anion radicals (·O$_2^-$) by electron spin resonance, further verifying the presence of a built-in electric field with generated piezopotentials under US irradiation (Fig. 3, C and D, and fig. S9, A and B) (41).

Construction of BTO@NOBac sabotages tumor by generation of peroxynitrite

The radical reaction between ·O$_2^-$ and NO generates potent RNS peroxynitrite with a half-life of ~10 ms (27). Then, BTO NPs were hybridized with NOBac to form a peroxynitrite generator through electrostatic interaction (Fig. 3E). Since both BTO NPs and NOBac were negatively charged (−1 and −42.0 mV, respectively), polyethyleneimine (PEI) was used to coat BTO NPs, making the BTO NPs positively charged (+6.23 mV) (Fig. 3F). PEI-BTO NPs were then attached to NOBac, yielding BTO@NOBac with uniform loading (Fig. 3G) and good biocompatibility (Fig. 3H and fig. S10). BTO@NOBac also displays the characteristic peak of BTO positioned at 1750 cm^{-1} and the characteristic of NOBac positioned at 2925 cm^{-1}. Specifically, characteristic peaks of 2925 and 1085 cm^{-1} can be ascribed to —COOH and —C—O of NOBac, respectively. Peaks of 1750 cm^{-1} can be ascribed to C=O of BTO NPs, collectively confirming the successful construction of BTO@NOBac (Fig. 3I). Generation of ONOO$^-$ by BTO@NOBac under US irradiation was evaluated by using l-tyrosine, which could be nitrated by ONOO$^-$ in the presence of carbon dioxide to give a fluorescent product [excitation wavelength (Ex) = 313 nm; emission wavelength (Em) = 406 nm] (Fig. 3J) (30). From the evaluation result, we found that neither NOBac nor BTO + US produces fluorescent substances. When US irradiation was applied to the solution containing BTO@NOBac, prominent excited fluorescence (Ex = 313 nm; Em = 406 nm) could be obtained, revealing the abundant generation of peroxynitrite (Fig. 3K). Furthermore, the feeding amount of the BTO NPs and NOBac was optimized on the basis of a series of hybridization experiments for varied BTO NP concentrations as well as the resultant performance in generation of peroxynitrite. We have confirmed that feeding of BTO NPs (1000 μg/ml) formulates the most powerful hybridized BTO@NOBac for ONOO$^-$ production for future application (figs. S11 and S12).
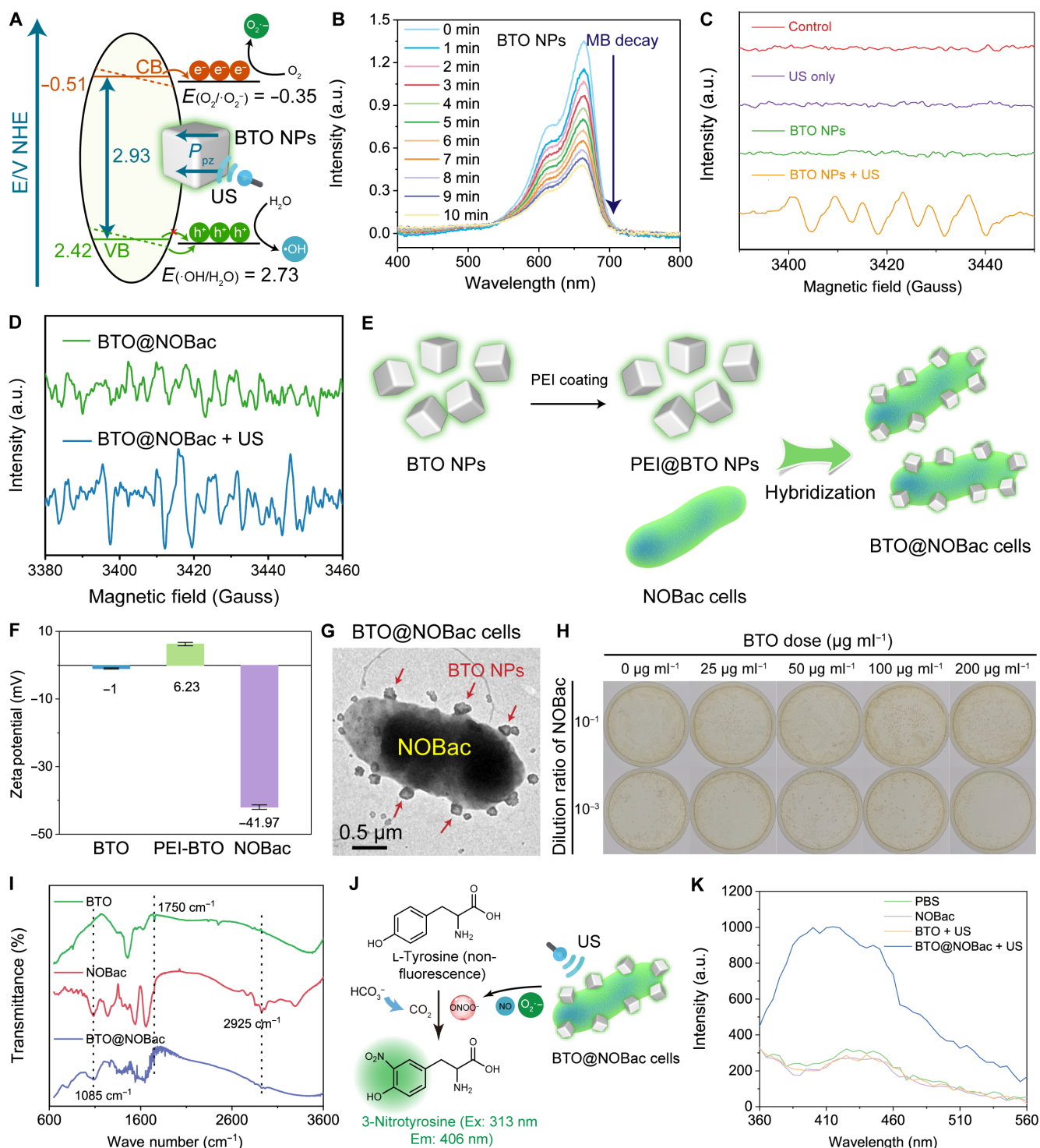
Fig. 3. Construction and investigation of BTO@NOBac. (**A**) Energy band configuration diagram of BTO nanoparticles. (**B**) Optical absorbance of MB degradation by BTO nanoparticles under US irradiation. (**C** and **D**) Electron spin resonance detections of superoxide anions generated by BTO nanoparticles (C) and BTO@NOBac (D) under US irradiation. (**E**) Schematic illustration of the construction of BTO@NOBac cells. (**F**) Zeta potentials of BTO, PEI-BTO, and NOBac. (**G**) TEM image of BTO@NOBac. (**H**) Photographs of LB agar plates of remaining NOBac after coincubation with BTO nanoparticles. (**I**) Fourier transform infrared spectra of BTO, NOBac, and BTO@NOBac. (**J**) Mechanism of the method for the detection of ONOO⁻ at solution level. (**K**) Fluorescence measurements of the generation of ONOO⁻.

In vitro antitumor evaluation by BTO@NOBac

We next used a murine breast tumor 4T1 cell line for cellular antitumor investigation. In a transwell system, 4T1 cells were seeded in the lower chamber, while BTO@NOBac was placed in the upper chamber for noncontact coincubation (Fig. 4A). We found that both WTBac and BTO NPs have good cytocompatibility against the cells, even at [Ba] in BTO NPs reaching 1000 µg/ml (fig. S13A) and the dose of WTBac being 10^8 CFU/ml (fig. S13B). When US irradiation was applied ($P = 1$ W/cm^2, $t = 5$ min) to BTO NPs, the relative cell viability (RCV) of 4T1 cells significantly reduced to 26.7% at [Ba] = 100 µg/ml (Fig. 4B). To determine the antitumor effect of NOBac, a microbe dose of 2×10^7 CFU/ml was applied, which leads to the overall destruction of the 4T1 cells (RCV = 17.2%), attributing to the prominent antitumor performance of NO during coincubation (Fig. 4C). After the conjugation of BTO NPs and NOBac, the obtained BTO@NOBac shows 21.4% of RCV at the dose of 10^7 CFU/ml (Fig. 4D), suggesting that BTO@NOBac is more cytotoxic than NOBac.

From confocal microscopic images, green fluorescence could be observed for 2′,7′-Dichlorofluorescin Diacetate (DCFH-DA)–stained 4T1 cells from NOBac, BTO + US, BTO@NOBac, and BTO@NOBac + US groups, while NO-specific DAF fluorescence could only be observed for 3-Amino,4-aminomethyl-2′,7′-difluorescein, diacetate (DAF-FM DA) stained cells from NOBac, BTO@NOBac, and BTO@NOBac + US groups (Fig. 4E). We also quantified the populations of the stained cells in flow cytometry. The population of DCF$^+$ cells increased from 17.3% (control group) to 27.3% (NOBac), 43.7% (BTO + US), and 59.3% (BTO@NOBac + US) (Fig. 4F and fig. S14A). While the population of DAF$^+$ cells increased from 1.95% (control group) to 7.40% (NOBac), 5.89% (BTO@NOBac), and 9.17% (BTO@NOBac + US) (Fig. 4G and fig. S14B). It is noted that the population of DAF$^+$ cells in the BTO@NOBac group is higher than that of the NOBac group, which may be attributed to the sonopiezo-generated hot electrons from BTO NPs that participate into the catalytic reaction of bNOS inside NOBac, thereby enhancing the production of NO from BTO@NOBac as compared to the primitive NOBac. These evidences collectively implicate the cellular oxidative stresses and generation of NO. We also used ONOO$^-$-specific fluorescence probe DAX-J2 to stain the cells and found green fluorescence exclusively from the cells treated with BTO@NOBac + US (Fig. 4E). On the basis of the intracellular identification of ROS/RNS, the cytotoxicity profiles for these treatments were further visualized. We used calcein acetoxymethyl ester/propidium iodide (calcein-AM/PI) dyes to stain 4T1 cells after respective treatments. Among control and all therapeutic groups, BTO@NOBac leads to the highest percentage of cell death upon US irradiation (Fig. 4E), indicating that the generated ONOO$^-$ outperforms other cell-killing reactive species such as NO and $\cdot O_2^-$.

Tumor tissues are in an immunosuppressed state, impeding traditional tumor immunotherapies. Activation of the immunosuppressed state of tumor can markedly improve the therapeutic outcomes (42). As a typical Gram-negative bacterium, NOBac is a promising candidate for stimulating native immunity including the polarization of macrophages (43, 44). After US irradiation, the cellular fragments of tumor and lipopolysaccharide (LPS) will release, respectively, from tumor cells and NOBac as tumor antigens. Then, the released LPS antigens were presented to DCs and macrophages, resulting in dendritic cell (DC) maturation and macrophage polarization to M1 type (Fig. 4H). We first evaluated the maturation of DCs induced by BTO@NOBac by quantifying the expression of CD80 and CD86. Compared to the minor DC maturation population in the control group (6.03%), significant increases in the maturation populations could be observed for BTO@NOBac and BTO@NOBac + 4T1 tumor cells + US group, which determined to be 37.1 and 55.3%, respectively (Fig. 4I). Chemotaxis of the macrophages is the primary hallmark of macrophage stimulation. In a transwell setup, macrophages were incubated in the upper chamber, while the stimulating substances after respective treatments (control, 4T1 tumor cells, BTO@NOBac, and BTO@NOBac + 4T1 tumor cells + US) were settled in the lower chamber (coincubation time of 24 hours). Crystal violet–stained macrophage in the upper chamber could be used to observe the migration of macrophage upon chemotaxis. For the control and 4T1 tumor cell groups without antigen releasing, slight amounts of stained macrophages could be seen. In contrast, BTO@NOBac coincubation stimulates the migration of macrophages, while the macrophages from BTO@NOBac + 4T1 tumor cells + US group can kill the most cancer cells and release tumor-associated antigens, thereby leading to the most prominently migrated macrophages stained with crystal violet, as observed under the microscopy (fig. S15). The M1-type macrophages exhibit an elongated fusiform morphology for engulfing and digesting pathogens compared to the round and flattened morphology of M2-type ones (45). Using phalloidine to stain the cell skeleton of the macrophages, we found that characteristic tentacles could be observed for cells in BTO@NOBac and BTO@NOBac + 4T1 tumor cells + US group. Such morphological changes indicate the substantial M1 polarization upon the corresponding treatments (Fig. 4J). In addition, CD86 as the marker of M1 polarization in RAW264.7 cells was used to analyze the phenotype of RAW264.7 cells with different treatments. Macrophage treated with 4T1 + BTO@NOBac + US has the most CD86$^+$ signal increase from 5.84% (control group) to 86.8% (BTO@NOBac + 4T1 + US group), which further illustrate that BTO@NOBac with US treatment could effectively promote the M1 polarization. M1 macrophage–related secretory cytokine was also detected by enzyme-linked immunosorbent assay. Macrophage in the group of 4T1 + BTO@NOBac + US secreted the highest amount of inflammatory cytokines such as interleukin-1β (IL-1β) and IL-6 (fig. S16). These results reveal that BTO@NOBac under the sonopiezodynamic treatment against 4T1 tumors could effectively promote the macrophage invasion and M1 polarization, meanwhile stimulating DC maturation for subsequent antigen presentation, overall presenting promising immunostimulating performance for both innate and adaptive immunity in vivo.

In vivo antitumor evaluation by BTO@NOBac

To evaluate the biosafety of BTO@NOBac for in vivo administration, we intravenously administrated four doses of BTO@NOBac (0, 5×10^6, 1×10^7, and 5×10^7 CFU/ml) to healthy Balb/c mice (female, 6 weeks old, $n = 3$). Within 30 days of evaluation timeframe, all mice survived, and the body weight of mice in each group shows no significant differences (fig. S17A). In addition, hematological indices (fig. S17B) and hematoxylin and eosin (H&E) staining of main organs (fig. S17C) of mice in different groups did not exhibit pathological abnormalities, revealing the satisfying biosafety of BTO@NOBac in vivo. We next investigated the tumor targeting performance of BTO@NOBac. Upon intravenous administration of BTO@NOBac at a dose of 10^8 CFU/ml to 4T1 xenograft–bearing nude mice (xenograft volume of approximately 300 mm^3), major organs including tumor
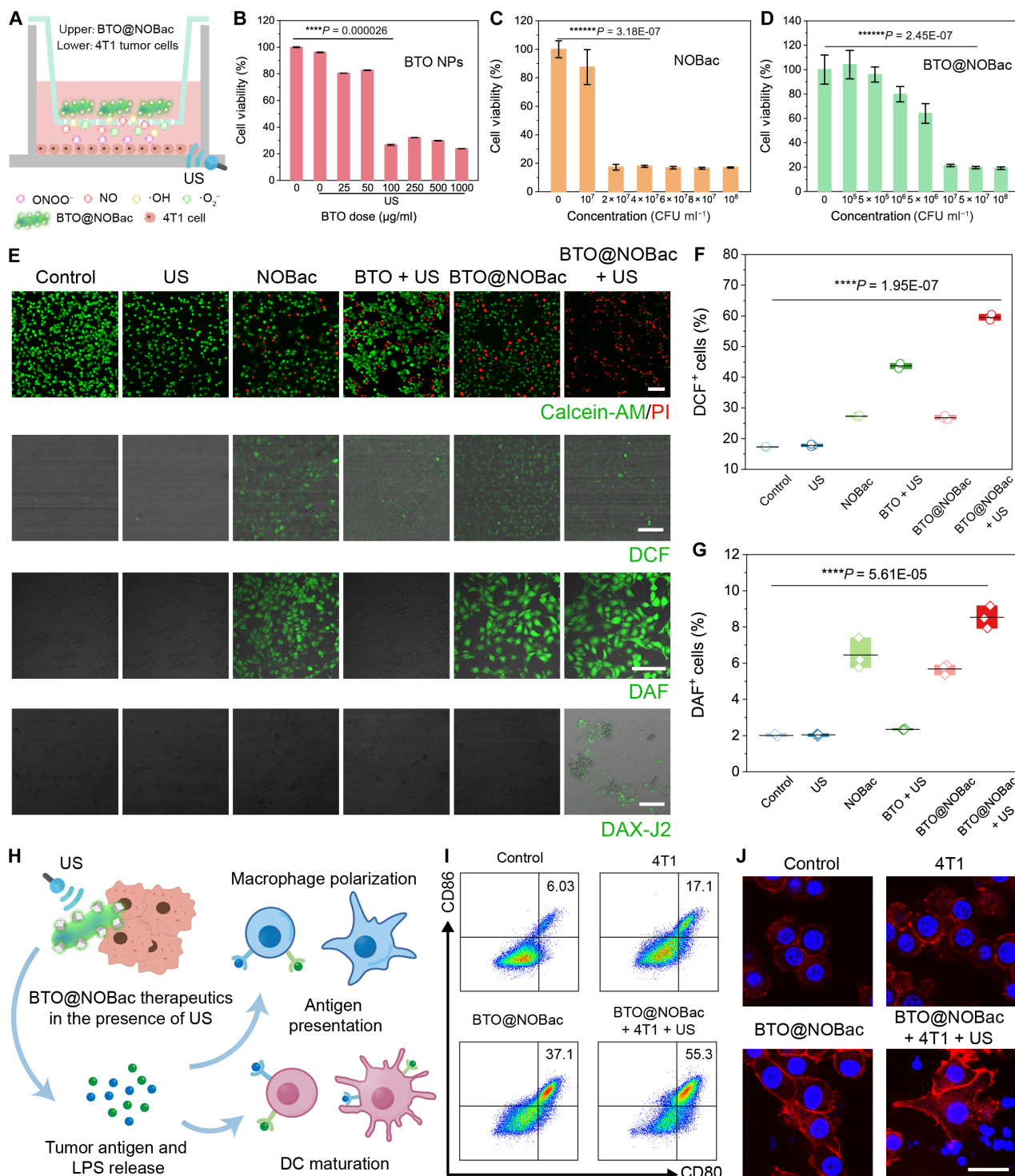
Fig. 4. In vitro therapeutic efficacy evaluation of BTO@NOBac. (**A**) Schematic diagram of the transwell setup for cellular experiments. (**B** to **D**) Cell viabilities of 4T1 cells cocultured with BTO NPs under US irradiation (B), NOBac (C), and BTO@NOBac under US irradiation (D). (**E**) Confocal microscopic images of 4T1 cells subjected to different treatments, followed by staining with calcein-AM/PI, DCFH-DA, DAF-AM, and DAX-J2, respectively. Scale bars, 100 μm. Percentages of DCF⁺ cells (**F**) and DAF⁺ cells (**G**) among 4T1 cells with different treatments by flow cytometric analyses. (**H**) Mechanism schematics of DC maturation and macrophage polarization, induced by the sonopiezo-catalytic therapeutic of BTO@NOBac. (**I**) Flow cytometry analysis of DC maturation (CD80CD86) after various treatments. (**J**) Confocal microscopic images of macrophages (phalloidine and 4′,6-diamidino-2-phenylindole dual-stained) after different treatments. Scale bar, 20 μm.

xenografts were harvested and homogenated at predetermined time points (6, 12, 24, and 48 hours) postinjection of BTO@NOBac, followed by subsequent plating and colony counting. We found that BTO@NOBac colonized only into the tumor region with especially high selectivity (fig. S18A). The number of colonies in tumor tissue in 48 hours postinjection was 63-fold that of the detected colony number in 6 hours postinjection, demonstrating that the therapeutic BTO@NOBac not only colonized but also proliferated in the tumor region, supporting and amplifying the NO generation performance and antitumor potentials (fig. S18B).

In vivo antitumor efficacy by BTO@NOBac was evaluated according to the planned therapeutic schedule (Fig. 5A). Thirty female Balb/c mice (6 weeks old) were randomly divided into six groups: control group, US group (US irradiation only), NOBac group (5×10^7 CFU/ml of NOBac, 100 μl), BTO + US group (2 mg/kg BTO NPs, US irradiation), BTO@NOBac group (5×10^7 CFU/ml of BTO@NOBac, 100 μl), and BTO@NOBac + US group (5×10^7 CFU/ml of BTO@NOBac, 100 μl, US irradiation). Intravenous administration

was conducted once a day on days 1, 3, and 5, while US irradiation was conducted on days 2, 4, and 6 (Fig. 5A). During the whole therapeutic evaluation period, the body weights of mice in each group showed no significant changes, indicating no acute toxicity of the treatment schedule (Fig. 5B). The dimensions of the xenograft from different groups were measured every 2 days. We found that xenografts of mice from the control and US groups grew constantly, with an average volume of the xenografts being 955 and 994 mm^3 on day 13. Xenografts of mice from NOBac, BTO + US, and BTO@NOBac groups increased much slower, respectively, to 471, 358, and 557 mm^3 finally. When mice were treated with BTO@NOBac + US, the xenograft growths were significantly suppressed as compared to control and other therapeutic groups (Fig. 5C and fig. S19). The tumor inhibition rate of BTO@NOBac + US group approaches 106%, much higher than other therapeutic groups (Fig. 5D). At the end of the therapeutic evaluation, mice were euthanized, and their tumors and main organs (heart, liver, spleen, lung, and kidney) were collected, photographed, and measured (Fig. 5E). According to the dissected
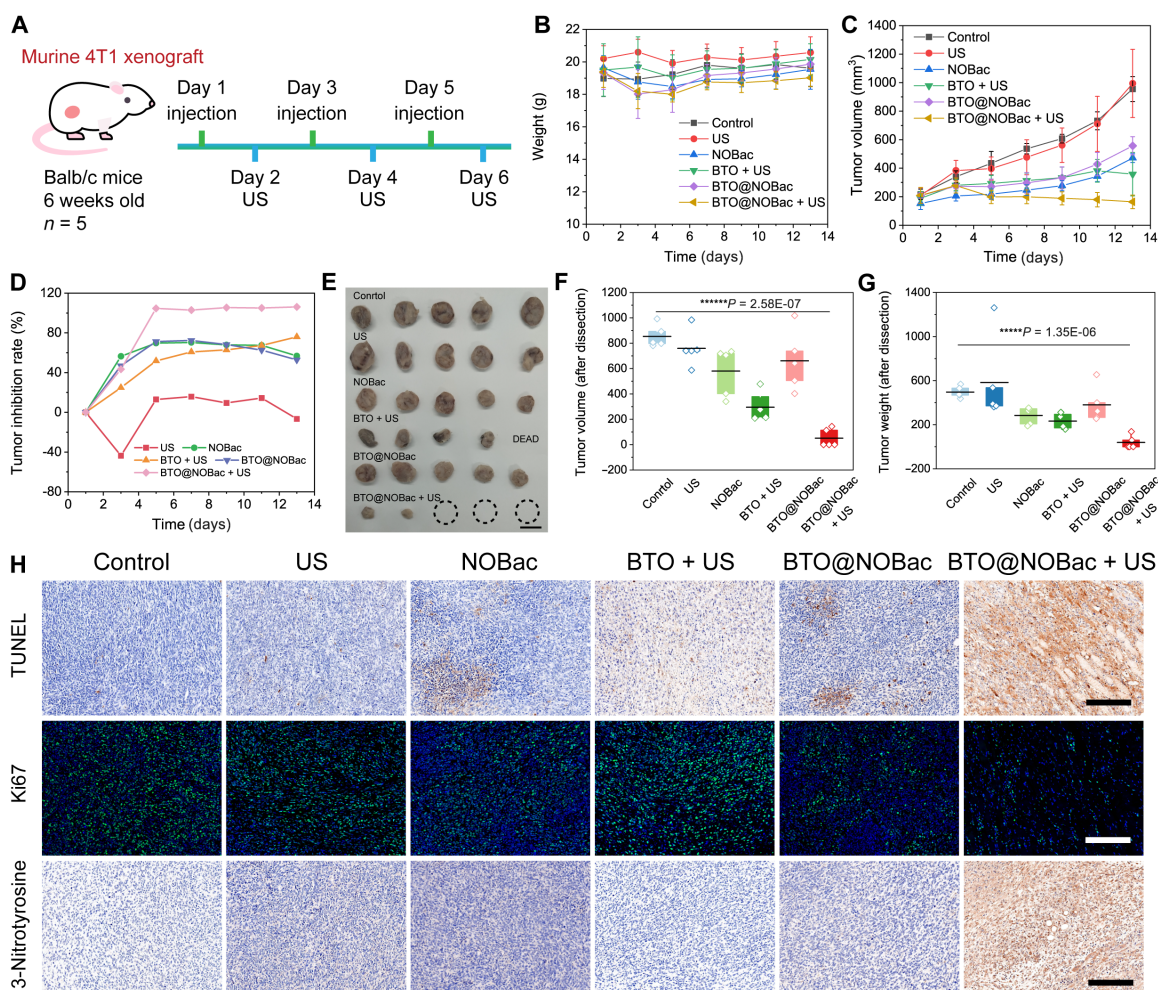
Fig. 5. In vivo evaluation of antitumor efficacy. (**A**) Schematic diagram of in vivo experimental procedure. (**B**) Body weight curves of mice recorded during the therapeutic timeframe. (**C**) Tumor growth curves of mice in different groups. (**D**) Tumor growth inhibition rate curves of mice in different groups. (**E**) Digital photograph of dissected tumors from mice in different groups. (**F**) Dissected tumor volumes of mice. (**G**) Tumor weights of mice in different groups after dissection. (**H**) Terminal deoxynucleotidyl transferase–mediated deoxyuridine triphosphate nick end labeling (TUNEL) staining, Ki67 immunofluorescence, and 3-nitrotyrosine (3-NT) immunohistochemistry staining of tumor tissues of mice in different groups. Scale bars, 200 μm.

tumor volumes and weights, significant therapeutic outcomes by BTO@NOBac + US could be validated (Fig. 5, F and G).

From the histological analyses of the dissected organs and tumors, no notable pathological abnormities could be observed in H&E staining sections of major organs from mice received different treatments (fig. S20), revealing no significant toxic side effect generated by these treatments. From the tumor section dissected from the BTO@NOBac + US group, negligible tumor nuclei, a large proportion of apoptotic cells as well as the suppressed cell proliferation could be observed, evidently indicating the outperformed therapeutic outcomes as compared to the other treatments (Fig. 5H and fig. S21). 3-Nitrotyrosine (3-NT) is a specific biomarker to indicate RNS such as peroxynitrite. A large population of 3-NT–positive nuclei could be observed in the tumor section of xenograft from BTO@NOBac + US group, validating the constant and prominent generation of the therapeutic peroxynitrite species from the synergetic interaction between BTO and NOBac (Fig. 5H).

BTO@NOBac stimulates the innate and adaptive immunity of antitumor

To investigate antitumor immunity activation by BTO@NOBac in the presence of US, 12 4T1 xenograft–bearing mice were randomly divided into four groups: control, NOBac, BTO + US, and BTO@NOBac + US groups. Intravenous administration and US irradiation were conducted on day 1 and day 2. On day 10, these mice were euthanized, and their spleen and tumor tissues were dissected, stained, and collected for multicolor flow cytometry (Fig. 6A). To better visualize the immunity regulation performance by the BTO@NOBac + US, t-distributed stochastic neighbor embedding (t-SNE) algorithm was applied to perform dimensionality reduction analysis on sample data (Fig. 6B) (46). According to the expressions of the cell markers including CD206, Ly-6G, CD3, CD62L, Nkp46, F4/80, CD80, CD49b, Ly-6G, CD11b, CD44, CD4, and CD8, nine types of the immune cells could be clustered based on the x-shift algorithm (Fig. 6C and fig. S22) and distributed on t-SNE maps with indicated islands [M1 bone marrow–derived macrophages (BMDMs), M1/M2 mix, M2 BMDMs, CD8+ T cells, CD4+ T cells, myeloid-derived suppressor cells (MDSCs), and other undefined cell types] (Fig. 6D). Their population distribution from the cells subjected to different treatments could then be mapped and quantified (Fig. 6E). MDSCs suppress broad types of immune responses such as T cell proliferation and cytokine generation, playing an important role in immunosuppression within cancer (47, 48). Signal dots of enhanced density is presented in the region of MDSCs for t-SNE maps of control, NOBac,
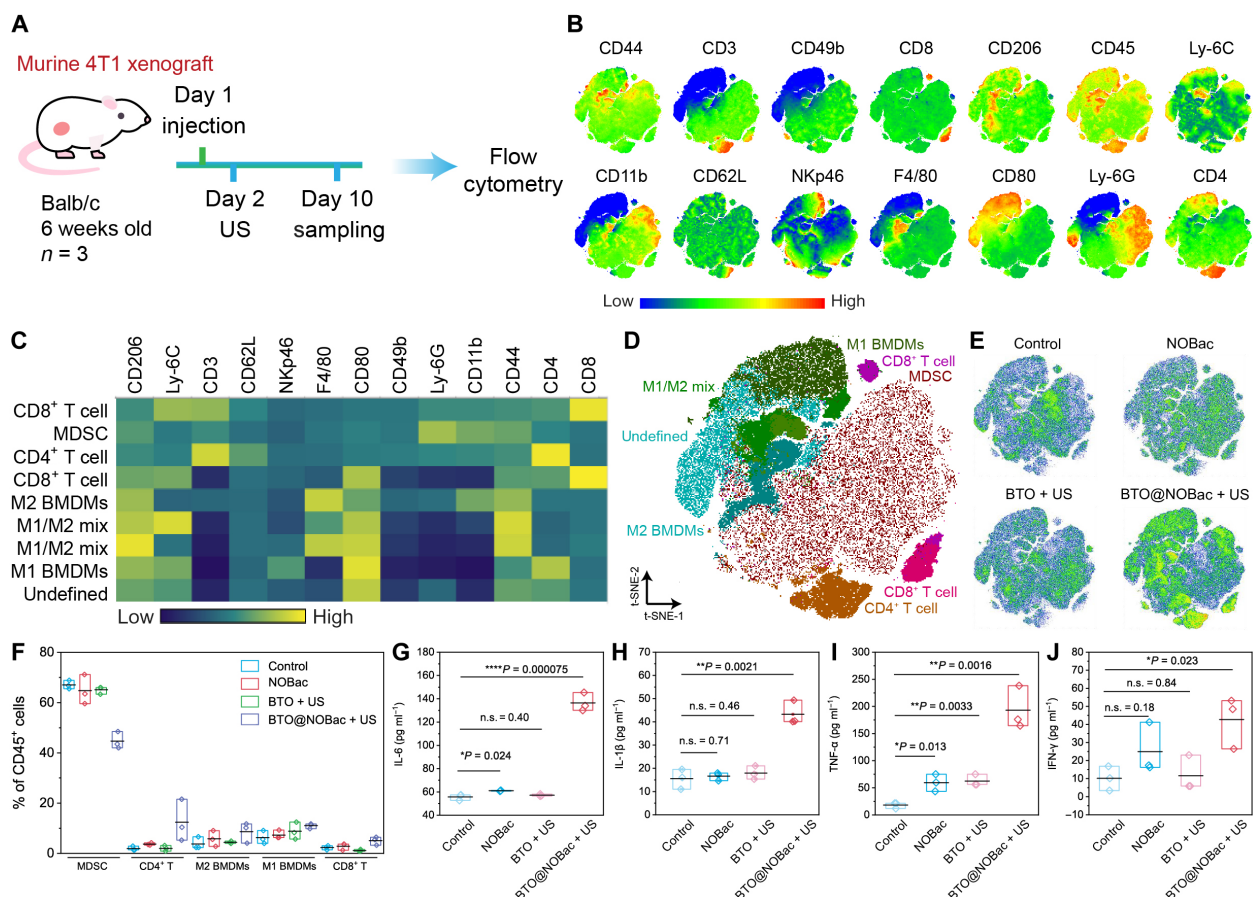
Fig. 6. Investigation of in vivo immune response. (**A**) Schematic treatment schedule of in vivo tumor fluorescence-activated cell sorting experiment. (**B**) Visualization of the expression of various cell markers in t-SNE. (**C**) Expressions of various cellular markers of x-shift clusters in heatmap. (**D**) Distribution of x-shift clusters on t-SNE maps. (**E**) Population distributions of different types of immune cells of tumor samples in different groups on t-SNE maps. (**F**) Percentages of different types of immune cells among CD45+ cells in each group. (**G** to **J**) Expression levels of IL-6 (G), IL-1β (H), tumor necrosis factor–α (TNF-α) (I), and interferon-γ (IFN-γ) (J) in serum samples of mice in different groups.

and BTO + US groups, suggesting that these tumors remain immunosuppressed. While signals of the same region of BTO@NOBac + US group are notably weaker, together with its much higher populations of CD4$^+$ T cells and CD8$^+$ T cells than those in other groups, indicating a notable antitumor immunoactivated microenvironment once treated with BTO@NOBac in the presence of US irradiation against tumor (Fig. 6E). Quantified percentages of each type of these immune cells among total CD45$^+$ cells reveal consistent results. The percentages of MDSC in control, NOBac, BTO + US, and BTO@NOBac + US groups are 67.0, 64.7, 65.1, and 44.7%, respectively, indicating the mitigated immunosuppressed status of tumors by BTO@NOBac + US treatment (Fig. 6F). In addition, BMDMs also play an important role in the immune-activation in tumor tissues. M2-polarized macrophages are incapable of antigen presentation and immunogenic tumor cell death, while M1-polarized macrophages exhibit antitumor effects (49). Compared to the control group (6.24%), the percentage of M1 macrophage of BTO@NOBac + US group is significantly increased (11.0%), which facilitates the clearance of dead cancer cells and subsequent presentation of antigens for immunostimulation (Fig. 6F). As the much more potent type of antigen-presenting cells, matured DCs (mDCs) have an enhanced migratory capacity, which is beneficial for antigen presentation and subsequent activation of T cells (50). Compared to the control group (21.0%), a higher population of CD80$^+$ CD86$^+$ mDCs could be quantified in the spleen tissues from BTO@NOBac + US group (35.9%; fig. S23). Upon potent antigen presentation, adaptive immunity could be effectively stimulated. The percentages of CD4$^+$ T cell and CD8$^+$ T cell in BTO@NOBac + US group are 12.4 and 5.05%, respectively, which are much higher than that of the control group (1.91% of CD4$^+$ T cell and 2.3% of CD8$^+$ T cell) (Fig. 6F). Immunofluorescence microscopic images of the tumor sections also reveal the presence of a majority of macrophages, DCs, and CD8$^+$ T cells, in the tumor tissue (fig. S21). Serum cytokines of mice from different groups are also assayed. Serum of mice from the BTO@NOBac + US group were detected of significantly augmented concentrations of IL-6, IL-1β, tumor necrosis factor–α, and interferon-γ cytokines, as compared to those of from control, NOBac, and BTO + US groups, demonstrating the whole-body activation of the immunity (Fig. 6, G to J).

We also investigated the long-term memory of adaptive immunity stimulated by BTO@NOBac. Memory T cells can be divided into central memory T cells (Tcm; CD44$^+$CD62L$^+$) and effector memory T cells (Tem; CD44$^+$CD62L$^-$), both of which can persist in the body for a long time period and provide long-term adaptive immune-protection (51, 52). In spleen lymphocytes (both CD4$^+$ and CD8$^+$) of control group, populations of Tcm and Tem were quantified to be 19.68 and 9.49%, respectively. Comparatively, these populations increased to 33.7 and 15.21%, respectively, in lymphocytes collected from the BTO@NOBac + US group, indicating the memory establishment of antitumor immunity after the treatment by BTO@NOBac + US (fig. S24).

DISCUSSION
In summary, we have constructed a hybridized and engineered BTO@NOBac by loading sonopiezosensitive BTO NPs onto the bNOS-encoding engineered probiotics NOBac, which is able to produce peroxynitrite under US irradiation for antitumoral living therapeutics. BTO@NOBac could generate NO gaseous molecules in a sustainable and more attractively amplifying manner (by 15.6-fold to the wide-type strain), which can subsequently react with O$_2^-$ generated by BTO NPs under US irradiation to produce abundant peroxynitrite ONOO$^-$ species in cascade. At a dose of 10^8 CFU/ml, BTO@NOBac could effectively eliminate 80.9% of 4T1 tumor cells by US-initiated peroxynitrite therapy, which is achieved synergistically by ONOO$^-$-induced cancer cell death and consequently potentiated immunoactivations through macrophage chemotaxis motivation, M1 phenotype polarization, as well as the maturation of DCs. In vivo vein injection of BTO@NOBac (5 × 10^7 CFU/ml) combined with US irradiation significantly inhibited progression of malignant tumors with an ultimate tumor inhibition rate of 106%, which are contributed majorly by the immunosuppressive tumor microenvironment reversion through destructing the immunosuppressive MDSCs, escalating the immunoactive M1 macrophages, mDCs, and activating effector T cells, as well as memory T cells. The present work establishes a paradigm of US-initiated sonopiezosensitive tumor therapeutic modality based on hybridized and engineered microbe, with concomitant stimulation of both innate and adaptive immunities, which is expected to benefit the design and development of novel high-performance antitumor therapeutics.

MATERIALS AND METHODS
Microbe strains and culture conditions
E. coli (strain MG1655 and strain DH5α) and *B. subtilis* were purchased from China Center of Industrial Culture Collection. LB broth was used for the microbe culture. Chloromycetin [25 μg/ml; Sangon Biotech (Shanghai) Co. Ltd.] was used in the antibiotic screening process of *E. coli*. Microbe concentration was determined by measuring the turbidity at optical density at 600 nm.

Plasmid construction and transformation
The shuttle plasmid backbone pYTK001 was derived from host *E. coli* strain DH5α with chloromycetin resistance. The DNA sequence of *bNOS* was extracted from the National Center for Biotechnology Information [GenBank: CP019663.1 (1092 bp) 836,438 to 837,529]. Gene fragments of *bnos* and plasmid backbone were amplified from templates in *B. subtilis* and *E. coli* strain DH5α, respectively, via PCR. A short histag protein (DNA sequences: 5′-caccatcatcaccatcac-3′) was used to label NOS protein. These obtained fragments were integrated into a complete plasmid [pYTK001-*bNOS*(6 × His)-CMR] through Gibson assembly. The obtained complete plasmids were introduced into competent *E. coli* strain MG1655 (WTBac) by heat shock transformation. Afterward, these microbes were smeared on LB agar plates with chloromycetin. These plates were cultured at 37°C overnight, and several monoclonal colonies were selected for sequencing by Sangon Biotech. Last, the single colony with the correct sequence (term NOBac) was used for further experiments.

Microbe Western blot
WTBac and NOBac (5 ml of overnight culture) were initially collected by centrifugation. Radioimmunoprecipitation assay lysis buffer (Beyotime, P0013B) was applied to lyse microbe, while the proteins in the supernatant were collected. After mixing with SDS–polyacrylamide gel electrophoresis protein loading buffer (YOBIBIO, UBI3006), the samples were denatured in a heating block and transferred to the polyvinylidene difluoride (PVDF) membrane (Beyotime, FFP24) after electrophoresis. Then, the PVDF membrane was immersed in TBST, a

mixture of tris-buffered saline (TBS) and polysorbate-20, solution (Beyotime, ST673) containing 5% skimmed milk powder for 1 hour. Next, the PVDF membrane was cultured with anti-Histag antibodies (1:1000; TransGen Biotech, HT501) or glyceraldehyde phosphate dehydrogenase (Abcam, ab125247) at 4°C overnight followed by 1-hour incubation with corresponding secondary antibody (1:2000; TransGen Biotech, HS201) at room temperature. Last, protein blots could be visualized in the presence of enhanced chemiluminescence (ECL) solution (Tanon, 180-506).

Measurements of NO generation

One milliliter of solution of LB broth, LB broth containing WTBac (10^7 CFU/ml), or LB broth containing NOBac (10^7 CFU/ml) was placed into the shaking incubator (37°C, 200 rpm) for predetermined periods (6, 12, and 24 hours). Then, their supernatants were separated and transferred into a 96-well plate through centrifugation (5000 rpm, 3 min). After the addition of the Griess reagent and the coincubation time of 10 min, the absorbance at 540 nm was measured by the plate reader. For fluorescence identification of NO, LB broth containing WTBac or NOBac was coincubated with the NO-specific fluorescence probe (DAF-FM-DA) for 30 min, followed by confocal observation.

Synthesis of BTO NPs

Ti[O(CH_2)$_3$$CH_3$]$_4$ (17.0 g) was dissolved into 20 ml of ethanol and then 7 ml of ammonium hydroxide solution (AR) and Ba hydroxide (14.2 g, dissolved in 25 ml of deionized water) were added into the above solution with stirring. The obtained suspension was then transferred into a Teflon-lined stainless-steel autoclave. The autoclave was sealed and heated at 200°C for 48 hours followed by naturally cooling down to room temperature. The resultant product was washed three times with acetic acid and ethanol, respectively, and dried under 80°C for 24 hours in an oven to yield cubic BTO NPs. To obtain tetragonal BTO NPs, cubic BTO NPs were further annealed at 800°C for 10 hours in air in a tube furnace.

MB bleaching assay

Twenty-five milligrams of BTO NPs was dispersed in 25 ml of methylene blue (MB) aqueous solution (10 mg/liter). After stirring in the dark overnight, the mixed solution was divided into five portions receiving US irradiation (1.0 MHz, 1 min, 50% duty cycle) with different irradiation power densities: 0, 0.5, 1, 1.5, and 2 W/cm^2. An infrared thermal imaging instrument was used to monitor the temperature changes of the mixed solutions during US irradiation. After US irradiation, the solutions were centrifuged with their supernatants collected and analyzed by UV-vis absorption spectroscopy at 400 to 800 nm.

Electron spin resonance assays

Five milliliters of 5,5-dimethyl-1-pyrroline-N-oxide was added to 100 μl of BTO aqueous solution (1 mg/ml). After mixing, US irradiation (1 MHz, 1 W/cm^2, 50% duty cycle, 1 min) was used to irradiate the solution. The solution was then transferred to a quartz tube, sealed, and placed into the electron paramagnetic resonance spectrometer for radical detection. For the detection of $\cdot O_2^-$, BTO NPs were dissolved into methanol, and 5-tert-butoxycarbonyl-5-methyl-1-pyrroline-N-oxide was applied as a trapping agent.

Hybridization of BTO NPs with NOBac

BTO NPs (5 ml, 1000 μg/ml) and PEI (100 μl, AR) aqueous solutions were mixed and stirred for 3 hours. The BTO-PEI NPs were rinsed with

deionized water three times and resuspended into the solution containing NOBac (2 ml, 10^8 CFU/ml) for further hybridization of 1 hour. The final product BTO@NOBac was obtained through centrifugation.

ONOO$^-$ fluorescence detection

The assay reagent for ONOO$^-$ detection was made by dissolving $NaHCO_3$ (630 mg) and l-tyrosine (4.36 mg) into 50 ml of phosphate-buffered saline (PBS). A solution containing NOBac, BTO NPs (200 μg/ml), or BTO@NOBac (10^8 CFU/ml) was redispersed into the assay reagent. US irradiation (for BTO + US group and BTO@NOBac + US group) parameters are set to 1 MHz, 1 W/cm^2, 50% duty cycle, 3 min. The resultant solution was lastly assayed in the microplate reader in the fluorescence mode (Ex: 313 nm, Em: 406 nm).

Cell culture and in vitro cytotoxicity experiments

The murine breast cancer cell line 4T1 was purchased from the Cell Bank, the Committee of Type Culture Collection of the Chinese Academy of Sciences. 4T1 cells were cultured in RPMI 1640 containing 10% fetal bovine serum (FBS) and 1% penicillin-streptomycin solution (10000 U ml^{-1}) in the incubator (37°C, 5% CO_2).

To investigate the in vitro cytotoxicity of BTO NPs or NOBac, 4T1 cells were seeded into 96-well plates and cultured with RPMI 1640 media with a density of 8000 cells per well for 12 hours for cell attachment. After rinsing the 4T1 cells with fresh PBS for three times, cells were coincubated with fresh media containing varied doses of BTO NPs [0, 25, 50, 100, 250, 500, and 1000 μg/ml, with or without US irradiation (1 MHz, 1 W/cm^2, 50% duty cycle, 5 min)] or NOBac (0, 10^7, 2×10^7, 4×10^7, 6×10^7, 8×10^7, and 10^8 CFU/ml) for 24 hours. Then, a standard cell counting kit-8 was applied to evaluate the cell viabilities of 4T1 cells with different treatments. The optical absorption was measured at 450 nm in the microplate reader.

Intracellular cell staining and visualization

Typically, 4T1 cells were seeded into lower chambers of a six-well transwell system (8×10^4 cells per well) and cultured for 12 hours. Subsequently, different treatments were applied to the cells: control group (untreated), US group (US irradiation only), NOBac group [NOBac (10^8 CFU/ml) was added into the upper chamber], BTO + US group [BTO NPs (60 μg/ml) were added to upper chamber followed by US irradiation], BTO@NOBac group [BTO@NOBac (10^8 CFU/ml) was added into the upper chamber], and BTO@NOBac + US group [BTO@NOBac (10^8 CFU/ml) was added into the upper chamber followed by US irradiation]. Afterward, cell staining probes were coincubated with the cells. For ROS staining: DCFH-DA (DOJINDO; Ex: 490 to 520 nm, Em: 510 to 540 nm). For intracellular NO staining: DAF-FM DA (Beyotime; Ex: 495 nm, Em: 515 nm). For intracellular ONOO$^-$ staining: DAX-J2 PON Green (AAT Bioquest Inc.; Ex: 490 nm, Em: 530 nm). For viable/dead cells staining: Calcein-AM (DOJINDO, Ex: 490 nm, Em: 515 nm) and PI (DOJINDO; Ex: 530 nm, Em: 580 nm). After coincubation, these cells were subjected to confocal observation (Olympus, FV1000). Flow cytometry was also used to quantify the fluorescence intensity of the stained cells (BD LSRFortessa).

In vivo antitumor therapeutic investigation

All animal experiments are guided by the Animal Care Ethics Commission of Shanghai Tenth People's Hospital (ID: SHDSYY-2022-Z0026). Thirty 4T1 xenograft–bearing mice were randomly divided into six groups ($n = 5$): control group (no treatment), US group (US irradiation only), NOBac group (100 μl of NOBac at the dose of 5×10^7 CFU/ml

was injected into each mouse), BTO + US group [mice were injected with BTO NPs (2.5 mg/kg) with US irradiation], BTO@NOBac group [mice were injected with BTO@NOBac (5×10^7 CFU/ml)], and BTO@NOBac + US group (mice were injected with BTO@NOBac with US irradiation). On days 1, 3, and 5, mice from NOBac, BTO + US, BTO@NOBac, and BTO@NOBac + US groups received respective administrations. Whereas US irradiation was performed on mice from US, BTO + US, and BTO@NOBac + US groups on days 2, 4, and 6. During the whole therapeutic period, mice were weighed, and the tumor dimensions were recorded every 2 days. On day 15, mice were euthanized, and tumor tissues as well as main organs were collected for histopathological analysis.

In vivo antitumor immunity investigation

Twelve 4T1 xenograft–bearing mice were randomly divided into four groups ($n = 3$): control group (no treatment), NOBac group (100 μl of NOBac at the dose of 5×10^7 CFU/ml was injected into each mouse), BTO + US group (mice were injected with BTO NPs (2.5 mg/kg) with US irradiation), and BTO@NOBac + US group (mice were injected with BTO@NOBac with US irradiation). On day 1, mice from NOBac, BTO + US, and BTO@NOBac + US groups received respective administrations. While US irradiation was performed on mice from BTO + US and BTO@NOBac + US groups on day 2, all mice were euthanized on day 10. Tumor tissues were dissected, scissored, and dissociated for single-cell isolation. The dissected spleen tissues were grounded with sterile syringes in fresh PBS and filtered with strainers. Afterward, these single-cell suspensions were centrifuged and resuspended in RBC lysis buffer for 5 min at room temperature. Subsequently, an equal volume of PBS (containing 10% FBS) buffers was applied to terminate the reaction. The cells were rinsed with fresh PBS twice followed by cell staining for fluorescence-activated cell sorting. Detailing staining procedures are documented in the Supplementary Materials.

Statistical analysis

Significances are calculated by Student's t test. n.s. indicates nonsignificant, $*P < 0.05$, $**P < 0.01$, $***P < 0.001$, and $****P < 0.0001$.

Supplementary Materials

This PDF file includes:
Supplementary Text
Figs. S1 to S24

REFERENCES AND NOTES

1. A. Rodrigo-Navarro, S. Sankaran, M. J. Dalby, A. del Campo, M. Salmeron-Sanchez, Engineered living biomaterials. *Nat. Rev. Mater.* **6**, 1175–1190 (2021).
2. D. W. Zheng, R. Q. Li, J. X. An, T. Q. Xie, Z. Y. Han, R. Xu, Y. Fang, X. Z. Zhang, Prebiotics-encapsulated probiotic spores regulate gut microbiota and suppress colon cancer. *Adv. Mater.* **32**, e2004529 (2020).
3. B. An, Y. Wang, Y. Huang, X. Wang, Y. Liu, D. Xun, G. M. Church, Z. Dai, X. Yi, T. C. Tang, C. Zhong, Engineered living materials for sustainability. *Chem. Rev.* **123**, 2349–2419 (2023).
4. T.-C. Tang, B. An, Y. Huang, S. Vasikaran, Y. Wang, X. Jiang, T. K. Lu, C. Zhong, Materials design by synthetic biology. *Nat. Rev. Mater.* **6**, 332–350 (2021).
5. X. Liu, M. E. Inda, Y. Lai, T. K. Lu, X. Zhao, Engineered living hydrogels. *Adv. Mater.* **34**, e2201326 (2022).
6. Y. Wang, Y. Liu, J. Li, Y. Chen, S. Liu, C. Zhong, Engineered living materials (ELMs) design: From function allocation to dynamic behavior modulation. *Curr. Opin. Chem. Biol.* **70**, 102188 (2022).
7. S. Li, Y. Zhang, S. H. Ho, B. Li, M. Wang, X. Deng, N. Yang, G. Liu, Z. Lu, J. Xu, Q. Shi, J. Y. Han, L. Zhang, Y. Wu, Y. Zhao, G. Nie, Combination of tumour-infarction therapy and chemotherapy via the co-delivery of doxorubicin and thrombin encapsulated in tumour-targeted nanoparticles. *Nat. Biomed. Eng.* **4**, 732–742 (2020).
8. D. Lu, L. Wang, L. Wang, L. An, M. Huo, H. Xu, J. Shi, Probiotic engineering and targeted sonoimmuno-therapy augmented by STING agonist. *Adv. Sci.* **9**, e2201711 (2022).
9. N. S. Forbes, Engineering the perfect (bacterial) cancer therapy. *Nat. Rev. Cancer* **10**, 785–794 (2010).
10. C. L. Ho, H. Q. Tan, K. J. Chua, A. Kang, K. H. Lim, K. L. Ling, W. S. Yew, Y. S. Lee, J. P. Thiery, M. W. Chang, Engineered commensal microbes for diet-mediated colorectal-cancer chemoprevention. *Nat. Biomed. Eng.* **2**, 27–37 (2018).
11. Y. E. Chen, D. Bousbaine, A. Veinbachs, K. Atabakhsh, A. Dimas, V. K. Yu, A. Zhao, N. J. Enright, K. Nagashima, Y. Belkaid, M. A. Fischbach, Engineered skin bacteria induce antitumor T cell responses against melanoma. *Science* **380**, 203–210 (2023).
12. J. H. Zheng, V. H. Nguyen, S. N. Jiang, S. H. Park, W. Tan, S. H. Hong, M. G. Shin, I. J. Chung, Y. Hong, H. S. Bom, H. E. Choy, S. E. Lee, J. H. Rhee, J. J. Min, Two-step enhanced cancer immunotherapy with engineered *Salmonella typhimurium* secreting heterologous flagellin. *Sci. Transl. Med.* **9**, eaak9537 (2017).
13. J. Li, Q. Xia, H. Guo, Z. Fu, Y. Liu, S. Lin, J. Liu, Decorating bacteria with triple immune nanoactivators generates tumor-resident living immunotherapeutics. *Angew. Chem. Int. Ed. Engl.* **61**, e202202409 (2022).
14. L. Wang, Z. Cao, M. Zhang, S. Lin, J. Liu, Spatiotemporally controllable distribution of combination therapeutics in solid tumors by dually modified bacteria. *Adv. Mater.* **34**, e2106669 (2022).
15. Y. Alapan, O. Yasa, O. Schauer, J. Giltinan, A. F. Tabak, V. Sourjik, M. Sitti, Soft erythrocyte-based bacterial microswimmers for cargo delivery. *Sci. Robot.* **3**, eaar4423 (2018).
16. D. W. Zheng, Y. Chen, Z. H. Li, L. Xu, C. X. Li, B. Li, J. X. Fan, S. X. Cheng, X. Z. Zhang, Optically-controlled bacterial metabolite for cancer therapy. *Nat. Commun.* **9**, 1680 (2018).
17. J. Li, X. Yu, Y. Jiang, S. He, Y. Zhang, Y. Luo, K. Pu, Second near-infrared photothermal semiconducting polymer nanoadjuvant for enhanced cancer immunotherapy. *Adv. Mater.* **33**, e2003458 (2021).
18. Y. Jiang, X. Zhao, J. Huang, J. Li, P. K. Upputuri, H. Sun, X. Han, M. Pramanik, Y. Miao, H. Duan, K. Pu, R. Zhang, Transformable hybrid semiconducting polymer nanozyme for second near-infrared photothermal ferrotherapy. *Nat. Commun.* **11**, 1857 (2020).
19. Y. Jiang, J. Li, X. Zhen, C. Xie, K. Pu, Dual-peak absorbing semiconducting copolymer nanoparticles for first and second near-infrared window photothermal therapy: A comparative study. *Adv. Mater.* **30**, 1705980 (2018).
20. N. Kang, S. Son, S. Min, H. Hong, C. Kim, J. An, J. S. Kim, H. Kang, Stimuli-responsive ferroptosis for cancer therapy. *Chem. Soc. Rev.* **52**, 3955–3972 (2023).
21. X. Qian, Y. Zheng, Y. Chen, Micro/nanoparticle-augmented sonodynamic therapy (SDT): Breaking the depth shallow of photoactivation. *Adv. Mater.* **28**, 8097–8129 (2016).
22. Y. Zhang, X. Zhang, H. Yang, L. Yu, Y. Xu, A. Sharma, P. Yin, X. Li, J. S. Kim, Y. Sun, Advanced biotechnology-assisted precise sonodynamic therapy. *Chem. Soc. Rev.* **50**, 11227–11248 (2021).
23. H. Xu, D. Kim, Y. Y. Zhao, C. Kim, G. Song, Q. Hu, H. Kang, J. Yoon, Remote control of energy transformation-based cancer imaging and therapy. *Adv. Mater.* **36**, 2402806 (2024).
24. H. Forgham, J. Zhu, X. Huang, C. Zhang, H. Biggs, L. Liu, Y. C. Wang, N. Fletcher, J. Humphries, G. Cowin, Multifunctional fluoropolymer-engineered magnetic nanoparticles to facilitate blood-brain barrier penetration and effective gene silencing in medulloblastoma. *Adv. Sci.* **11**, 2401340 (2024).
25. G. Ferrer-Sueta, N. Campolo, M. Trujillo, S. Bartesaghi, S. Carballal, N. Romero, B. Alvarez, R. Radi, Biochemistry of peroxynitrite and protein tyrosine nitration. *Chem. Rev.* **118**, 1338–1408 (2018).
26. P. Pacher, J. S. Beckman, L. Liaudet, Nitric oxide and peroxynitrite in health and disease. *Physiol. Rev.* **87**, 315–424 (2007).
27. C. Szabo, H. Ischiropoulos, R. Radi, Peroxynitrite: Biochemistry, pathophysiology and development of therapeutics. *Nat. Rev. Drug Discov.* **6**, 662–680 (2007).
28. Z. Wang, M. Zhan, W. Li, C. Chu, D. Xing, S. Lu, X. Hu, Photoacoustic cavitation-ignited reactive oxygen species to amplify peroxynitrite burst by photosensitization-free polymeric nanocapsules. *Angew. Chem. Int. Ed. Engl.* **60**, 4720–4731 (2021).
29. Z. Mao, J. Xiong, P. Wang, J. An, F. Zhang, Z. Liu, J. Seung Kim, Activity-based fluorescence probes for pathophysiological peroxynitrite fluxes. *Coord. Chem. Rev.* **454**, 214356 (2022).
30. S. Liu, W. Li, Y. Zhang, J. Zhou, Y. Du, S. Dong, B. Tian, L. Fang, H. Ding, S. Gai, P. Yang, Tailoring silica-based nanoscintillators for peroxynitrite-potentiated nitrosative stress in postoperative radiotherapy of colon cancer. *Nano Lett.* **22**, 6409–6417 (2022).
31. P. Zhu, Y. Chen, J. Shi, Piezocatalytic tumor therapy by ultrasound-triggered and BaTiO₃-mediated piezoelectricity. *Adv. Mater.* **32**, e2001976 (2020).
32. H.-W. Lee, S. Moon, C.-H. Choi, D. K. Kim, S. J. Kang, Synthesis and size control of tetragonal barium titanate nanopowders by facile solvothermal method. *J. Am. Ceram. Soc.* **95**, 2429–2434 (2012).
33. S.-Y. Jun, S. H. Park, M. K. Sohn, S. Kim, J. M. Lee, D. S. Kong, T.-Y. Lee, J. H. Jung, M.-S. Kim, S. Yoo, J.-H. Ko, S. Cha, D. Jung, J.-Y. Kim, S. Yu, Reduction time effect on the dielectric characteristics of reduced-graphene-oxide–encapsulated barium titanate powder fillers. *Carbon* **199**, 23–32 (2022).
34. J. Narvaez, F. Vasquez-Sancho, G. Catalan, Enhanced flexoelectric-like response in oxide semiconductors. *Nature* **538**, 219–221 (2016).

35. M. Li, L. Zhang, X. Fan, M. Wu, Y. Du, M. Wang, Q. Kong, L. Zhang, J. Shi, Dual synergetic effects in MoS$_2$/pyridine-modified g-C$_3$N$_4$ composite for highly active and stable photocatalytic hydrogen evolution under visible light. *Appl. Catal. B Environ.* **190**, 36–43 (2016).

36. H. Xue, L. Jiang, G. Lu, J. Wu, Multilevel structure engineered lead-free piezoceramics enabling breakthrough in energy harvesting performance for bioelectronics. *Adv. Func. Mater.* **33**, 2212110 (2022).

37. Y. Zhao, T. Huang, X. Zhang, Y. Cui, L. Zhang, L. Li, Z. L. Wang, Piezotronic and piezo-phototronic effects on sonodynamic disease therapy. *BMEMat* **1**, e12006 (2023).

38. J. Wu, Q. Xu, E. Lin, B. Yuan, N. Qin, S. K. Thatikonda, D. Bao, Insights into the role of ferroelectric polarization in piezocatalysis of nanocrystalline BaTiO$_3$. *ACS Appl. Mater. Interfaces* **10**, 17842–17849 (2018).

39. D. A. Armstrong, R. E. Huie, W. H. Koppenol, S. V. Lymar, G. Merényi, P. Neta, B. Ruscic, D. M. Stanbury, S. Steenken, P. Wardman, Standard electrode potentials involving radicals in aqueous solution: Inorganic radicals (IUPAC Technical Report). *Pure Appl. Chem.* **87**, 1139–1150 (2015).

40. Y. Feng, P. H. Lee, D. Wu, Z. Zhou, H. Li, K. Shih, Degradation of contaminants by Cu$^+$-activated molecular oxygen in aqueous solutions: Evidence for cupryl species (Cu^{3+}). *J. Hazard. Mater.* **331**, 81–87 (2017).

41. Q. Wu, H. Zhang, H. Liu, External physical field-driven nanocatalytic cancer therapy. *BMEMat* **1**, e12010 (2023).

42. K. Cheng, R. Zhao, Y. Li, Y. Qi, Y. Wang, Y. Zhang, H. Qin, Y. Qin, L. Chen, C. Li, J. Liang, Y. Li, J. Xu, X. Han, G. J. Anderson, J. Shi, L. Ren, X. Zhao, G. Nie, Bioengineered bacteria-derived outer membrane vesicles as a versatile antigen display platform for tumor vaccination via Plug-and-Display technology. *Nat. Commun.* **12**, 2041 (2021).

43. B. W. Simpson, M. S. Trent, Pushing the envelope: LPS modifications and their consequences. *Nat. Rev. Microbiol.* **17**, 403–416 (2019).

44. Y. Yang, M. B. Torchinsky, M. Gobert, H. Xiong, M. Xu, J. L. Linehan, F. Alonzo, C. Ng, A. Chen, X. Lin, A. Sczesnak, J. J. Liao, V. J. Torres, M. K. Jenkins, J. J. Lafaille, D. R. Littman, Focused specificity of intestinal TH17 cells towards commensal bacterial antigens. *Nature* **510**, 152–156 (2014).

45. Y. Guo, Q. Bao, P. Hu, J. Shi, Nanomedicine-based co-delivery of a calcium channel inhibitor and a small molecule targeting CD47 for lung cancer immunotherapy. *Nat. Commun.* **14**, 7306 (2023).

46. S. Toghi Eshghi, A. Au-Yeung, C. Takahashi, C. R. Bolen, M. N. Nyachienga, S. P. Lear, C. Green, W. R. Mathews, W. E. O'Gorman, Quantitative comparison of conventional and t-SNE-guided gating analyses. *Front. Immunol.* **10**, 1194 (2019).

47. J. I. Youn, D. I. Gabrilovich, The biology of myeloid-derived suppressor cells: The blessing and the curse of morphological and functional heterogeneity. *Eur. J. Immunol.* **40**, 2969–2975 (2010).

48. D. I. Gabrilovich, Myeloid-derived suppressor cells. *Cancer Immunol. Res.* **5**, 3–8 (2017).

49. L. Wu, X. H. Zhang, Tumor-associated neutrophils and macrophages-heterogenous but not chaotic. *Front. Immunol.* **11**, 553967 (2020).

50. Y. Wang, Y. Xiang, V. W. Xin, X. W. Wang, X. C. Peng, X. Q. Liu, D. Wang, N. Li, J. T. Cheng, Y. N. Lyv, S. Z. Cui, Z. Ma, Q. Zhang, H. W. Xin, Dendritic cell biology and its role in tumor immunotherapy. *J. Hematol. Oncol.* **13**, 107 (2020).

51. D. Ojdana, K. Safiejko, A. Lipska, P. Radziwon, J. Dadan, E. Tryniszewska, Effector and memory CD4$^+$ and CD8$^+$ T cells in the chronic infection process. *Folia Histochem. Cytobiol.* **46**, 413–417 (2008).

52. W. Ratajczak, P. Niedzwiedzka-Rystwej, B. Tokarz-Deptula, W. Deptula, Immunological memory cells. *Cent. Eur. J. Immunol.* **43**, 194–203 (2018).